

Divergence-Free Shape Interpolation and Correspondence

MARVIN EISENBERGER, Technical University of Munich, Germany

ZORAH LÄHNER, Technical University of Munich, Germany

DANIEL CREMERS, Technical University of Munich, Germany

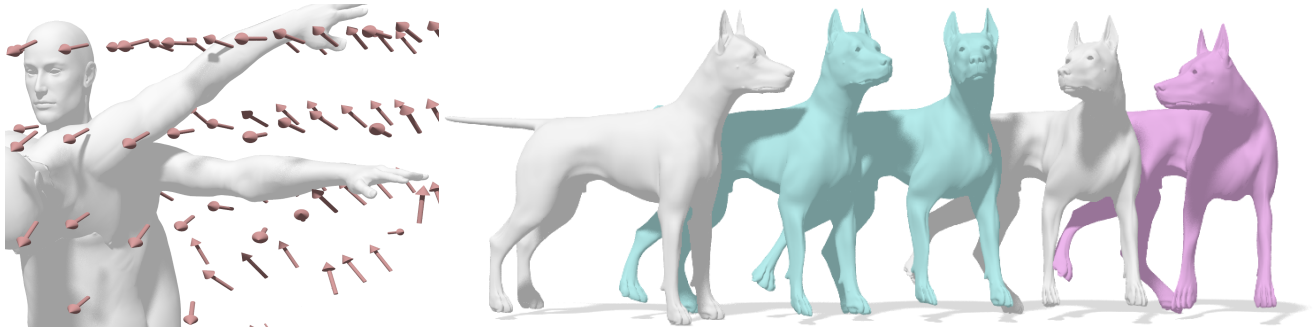


Fig. 1. Given two input shapes we propose to compute a volume-preserving deformation field by imposing a zero-divergence constraint. The resulting method alternates between optimizing the deformation field and calculating a correspondence for a small subset of vertices. (Left) Example of a deformation field in 3D. (Right) Our approach generates a continuous family of intermediate shapes along with a highly accurate correspondence. The input shapes are shown in white, intermediate shapes in blue and one extrapolation is shown in pink.

We present a novel method to model and calculate deformation fields between shapes embedded in \mathbb{R}^D . Our framework combines naturally interpolating the two input shapes and calculating correspondences at the same time. The key idea is to compute a divergence-free deformation field represented in a coarse-to-fine basis using the Karhunen-Loève expansion. The advantages are that there is no need to discretize the embedding space and the deformation is volume-preserving. Furthermore, the optimization is done on downsampled versions of the shapes but the morphing can be applied to any resolution without a heavy increase in complexity. We show results for shape correspondence, registration, inter- and extrapolation on the TOSCA and FAUST data sets.

ACM Reference Format:

Marvin Eisenberger, Zorah Lähner, and Daniel Cremers. 2022. Divergence-Free Shape Interpolation and Correspondence. 1, 1 (June 2022), 14 pages. https://doi.org/0000001.0000001_2

1 CHALLENGES IN SHAPE ANALYSIS

Handling non-rigidly deformed versions of a 3D shape is at the heart of numerous problems in computer vision and graphics ranging from shape comparison, information and style transfer to the

Authors' addresses: Marvin Eisenberger, Technical University of Munich, Boltzmannstrasse 3, Garching, 85748, Germany, marvin.eisenberger@in.tum.de; Zorah Lähner, Technical University of Munich, Boltzmannstrasse 3, Garching, 85748, Germany, laehner@in.tum.de; Daniel Cremers, Technical University of Munich, Boltzmannstrasse 3, Garching, 85748, Germany, cremers@tum.de.

Permission to make digital or hard copies of all or part of this work for personal or classroom use is granted without fee provided that copies are not made or distributed for profit or commercial advantage and that copies bear this notice and the full citation on the first page. Copyrights for components of this work owned by others than ACM must be honored. Abstracting with credit is permitted. To copy otherwise, or republish, to post on servers or to redistribute to lists, requires prior specific permission and/or a fee. Request permissions from permissions@acm.org.

© 2022 Association for Computing Machinery.
XXXX-XXXX/2022/6-ART \$15.00
https://doi.org/0000001.0000001_2

automatic generation of new but meaningful shapes. In contrast to rigid deformations which lead to a problem with six degrees of freedom, the complexity for non-rigid formulations normally grows quadratically with the number of vertices in the input shapes.

While many of these tasks are intrinsically related most existing methods address them independently and do not generalize to a wider range of problems. For example, having the same texture on both input shapes can help to find correspondences between these, while knowing the correspondence makes it easy to transfer the texture. Doing joint optimization can help to improve the performance in both tasks. Our approach combines shape registration, correspondence and interpolation which bring different viewpoints to the same question of how two non-rigidly deformed input shapes relate to each other.

Shape registration aims at finding a transformation of a shape \mathcal{X} that will align its surface with another shape \mathcal{Y} as closely as possible. This is trivial when the *correspondence* $\pi : \mathcal{X} \rightarrow \mathcal{Y}$ is already given, because then we can prescribe a deformation which aligns each point $x \in \mathcal{X}$ with its match $\pi(x) = y \in \mathcal{Y}$. Vice versa, when two surfaces are aligned, a correspondence can easily be found by searching for the nearest neighbor of each point in the embedding space. The *shape interpolation* problem addresses the task of finding a sequence of intermediate shapes between \mathcal{X} and \mathcal{Y} such that \mathcal{X} is transformed into \mathcal{Y} in a natural and continuous way. Most methods tackling this task assume they are given a perfect correspondence between the initial shapes but the possibility of a smooth transition is actually a requirement for a good correspondence.

Many state-of-the-art correspondence methods can find fairly accurate matchings but they often rely on pointwise information like descriptor values or pairwise distances. While these are straight forward to compute, information about continuity is not encoded or increases the complexity of the optimization heavily. Consequently,

outliers due to intrinsic symmetries or different sampling prevent a continuous morphing. A representation that can formulate both problems and makes a joint optimization possible is needed.

2 RELATED WORK

2.1 Deformation Fields

Deformation fields have a long history in image registration. Ashburner and colleagues made use of deformation fields for autonomous shape morphing [Ashburner 2007]. They consider temporally constant deformation fields offering limited flexibility to capture more complex deformations. Solving for a space and time dependent deformation field is a highly underdetermined problem. A remedy for this issue is provided by the geodesic shooting approach advocated by [Miller et al. 2006] which only estimates the initial velocity field for each pixel and then how the velocity has to propagate in the image domain in order to preserve the kinetic energy and the momentum of the whole system. Further improvements of this framework were proposed in subsequent work, including a Gauss-Newton approach [Ashburner and Friston 2011] and a particularly efficient adjoint calculation [Vialard et al. 2012].

It is often beneficial to have a probabilistic interpretation of deformation fields. This yields a comprehensive description with explicit schemata to impose uniformity on vector fields as well as a sound theoretical foundation. Such a model for image registration and 2D shape registration with a Gaussian process modeling of the correspondence mapping is proposed in [Albrecht et al. 2008]. Further work [Dölz et al. 2017; Lüthi et al. 2016] specified how one can extend this approach to Gaussian processes on the surface of a three dimensional shape. The authors in [Bregler et al. 2000], [Torresani et al. 2008], [Albrecht et al. 2008] and [Paladini et al. 2009] also model non-rigid transformations using a PCA type representation of permitted motions. Analogously, [Myronenko and Song 2010] and [Ma et al. 2014] pursue a reproducing kernel Hilbert space approach to model the vector field interpolation. However, for all these references the respective vector fields are not defined on the whole surrounding space of the shapes but rather only at the elements of the considered point clouds and they do not admit an interpretation as a deformation field.

2.2 Shape Registration and Matching

Much work has been done in the direction of shape registration and matching and we would like to point the interested reader to in-depth surveys of these topics for an overview [Salvi et al. 2007; Tam et al. 2013; van Kaick et al. 2011]. Here we will focus on work that is directly related to our approach.

A popular line of work in shape matching is based on spectral decomposition of the surface Laplace-Beltrami operator [Dubrovina and Kimmel 2010]. This is popular because it reduces the dimensionality of the problem from the number of vertices to the number of basis functions chosen [Ovsjanikov et al. 2012]. Nevertheless, extracting the correspondence from the low dimensional representation is still a complex problem and often retrieved solutions are noisy or hard to compute [Rodolà et al. 2015]. We also use a spectral approach but, instead of a basis for functions on the surface, we

represent deformation fields in the embedding space which results in a natural formulation for the correspondence retrieval.

Methods based on Multi-Dimensional Scaling find correspondences by reembedding and then aligning shapes in a (possibly smaller) embedding space where the complexity is reduced [Aflalo et al. 2016; Bronstein et al. 2006]. [Chen and Koltun 2015] calculate a robust non-rigid registration based on Markov random fields but can not retrieve a continuous deformation. In [Myronenko and Song 2010] and [Ma et al. 2014] the authors address the non-rigid registration problem by modeling one point cloud as a Gaussian mixture model. Moreover, they also determine the correspondences and point mappings in an alternating manner using a expectation maximization algorithm. This work is strongly related to our framework. Like our approach they directly model the correspondence mapping of all points as a Gaussian process type mapping. We will show later that this can actually be interpreted as a particular instance of the method we propose here.

2.3 Shape Interpolation

Although registration methods often compute a deformation between shapes, the focus is not on producing realistic intermediate shapes. Most methods realistically interpolating between shapes assume to be given a full correspondence in advance. [Wirth et al. 2011] and [Heeren et al. 2016] model a space of shells with metrics induced by physical deformation energies in which geodesics or splines represent natural interpolations between shells. [Von-Tycowicz et al. 2015] make real-time interpolation on a set of pre-processed, given shapes with arbitrary resolution possible.

[Alexa et al. 2000] only needs a handful of correct correspondences to find a volume-preserving deformation between two shapes but they require both to be segmented in compatible simplicial complexes. In [Xu et al. 2005] a dense deformation field similar to ours is calculated but the method depends on a consistent triangulation of the inputs. Other directions include taking user input to guide deformations in the right direction [Vaxman et al. 2015] or rely on a known or learned model to generate new shapes [Gao et al. 2017].

3 CONTRIBUTION

In the following, we will introduce a mathematical framework which allows to jointly tackle the problems of shape interpolation/extrapolation, shape registration and correspondence estimation. Given two 3D shapes we propose to estimate a smooth and volume-preserving 3D deformation field creating a plausible interpolation of these shapes. More specifically, we solve an initial value problem for determining the shape deformation. This framework allows us to incorporate physical assumptions about the deformation field. We suggest to impose volume preservation by enforcing zero divergence. More specifically, we represent the deformation field as the curl of a potential function and propose a natural coarse-to-fine basis representation of these potential functions. The initial value problem is then solved by an explicit Euler scheme. We use an expectation maximization approach to simultaneously determine a subset of the unknown point-to-point correspondences and the optimal deformation field parameters. The objective is aligning two

shapes with a preferably uniform deformation field. We demonstrate that the proposed framework can be used to create plausible shape interpolations and extrapolations in numerous experiments. Moreover, it provides a shape correspondence which compares to state-of-the-art correspondence methods.

4 PROBLEM FORMULATION

This section gives an introduction into the problem we want to solve and the mathematical background we use in later sections.

4.1 Deformation field shape correspondences

Consider two discrete sets of points $\mathcal{X} = \{x_1, \dots, x_N\} \subset \Omega$ and $\mathcal{Y} = \{y_1, \dots, y_M\} \subset \Omega$ contained in a compact domain $\Omega \subset \mathbb{R}^D$. The points x_n and y_m are assumed to be uniformly sampled from the surface of two similar D -dimensional shapes. The shape registration problem now addresses the task of aligning the point clouds \mathcal{X} and \mathcal{Y} in a meaningful manner, such that similar regions of the two shapes are matched onto each other. In analogy to the approach in [Ma et al. 2014] we are looking for a correspondence mapping $f : \Omega \rightarrow \mathbb{R}^D$, such that the mapped points $f(x_n)$ fit to the sample set \mathcal{Y} .

Our approach chooses these mappings f in such a way that they imitate plausible transformations in the real world. For this purpose we make some natural assumptions about the trajectories of the transformed points x_n . For once we require the points of our shape to move smoothly over time. We would also like points in a certain neighborhood to shift in a uniform manner. This assumption yields to some extent that the determined correspondences are continuous. Moreover, the volume of shifted objects should remain the same. We therefore assume that every point $x_n \in \mathcal{X}$ moves according to the following initial value problem:

$$\begin{cases} \dot{x}(t) = v(x(t)). \\ x(0) = x_n. \end{cases} \quad (1)$$

In this context $v : \Omega \rightarrow \mathbb{R}^D$ is some fixed deformation field moving the point x_n over time. In order to ensure a uniform movement of the samples the vector field v has to be sufficiently smooth. We will even assume that $v \in C^\infty(\Omega, \mathbb{R}^D)$, which yields the following well-known result:

PROPOSITION 1. *For a deformation field $v \in C^\infty(\Omega, \mathbb{R}^D)$, the initial value problem (1) admits a solution on the compact domain Ω and this solution is unique.*

PROOF. This follows directly from the theorem of Picard-Lindelöf [Teschl 2012, Theorem 2.5]. \square

As a consequence we can choose the correspondence mapping f to be the solution operator of (1) evaluated at an arbitrary time t . For convenience we choose $t = 1$:

$$f : \begin{cases} \Omega \rightarrow \mathbb{R}^D. \\ x_n \mapsto x(1). \end{cases} \quad (2)$$

But our strict assumptions about the deformation field v yield an even stronger regularity for the trajectories resulting from (1):

PROPOSITION 2. *The unique solution to (1) is infinitely many times continuously differentiable, i.e. $x \in C^\infty([0, 1], \mathbb{R}^D)$.*

PROOF. This follows from [Teschl 2012, Lemma 2.3]. \square

The advantage of this framework is that it provides an intuitive notion of deformation when analyzing shape correspondences. Therefore, one does not only get a matching of two shapes but also all intermediate states constituting the underlying transformation. Those are typically more meaningful than merely performing linear interpolation between the initial and the final position of each point x_n . Especially when looking at nearly isometric shapes having a continuous correspondence and a natural deformation are inherently connected and solving for both simultaneously improves the results considerably.

4.2 Divergence free deformations

Another convenient quality of the presented framework is that it enables us to incorporate assumptions about the deformation field into our model. One reasonable restriction arises from the mathematical investigation of fluid dynamics [Chorin and Marsden 1993], namely the restriction to divergence free velocity fields:

$$\nabla \cdot v = 0. \quad (3)$$

It is well known that this local property confines the vector field in such a way, that it yields volume conservation over time for any considered part $U \subset \Omega$ of the shape:

PROPOSITION 3. *Consider an open set $U \subset \Omega$. Let now $U(t)$ be the set of solutions of (1), if any point in U is shifted individually. If we assume that the deformation field v is divergence-free (3), then the volume of $U(t)$ is constant over time:*

$$\frac{d}{dt} \int_{U(t)} dx = 0. \quad (4)$$

PROOF. This statement is a particular case of the result in [Teschl 2012, Lemma 8.8]. \square

Helmholtz's theorem [Aris 1962] implies that any sufficiently smooth vector field on the compact domain Ω can be decomposed into the sum of a curl free and a divergence free component. It furthermore provides us with an explicit construction of the divergence free component of any velocity field:

$$v := \nabla \times \Phi. \quad (5)$$

In this context, $\Phi : \Omega \rightarrow \mathbb{R}^D$ is a C^∞ potential field. This vector field Φ arises from a construction in the Helmholtz decomposition and it typically depends on the considered vector field v . Unfortunately constructing Φ from v is not straightforward and it is in general not computationally feasible. Therefore we allow the potential Φ to be an arbitrary vector field. Then we can define v to be its curl in analogy to (5). Either way we get a divergence free vector field v due to the following basic property of the curl operator:

$$\nabla \cdot (\nabla \times \Phi) = 0. \quad (6)$$

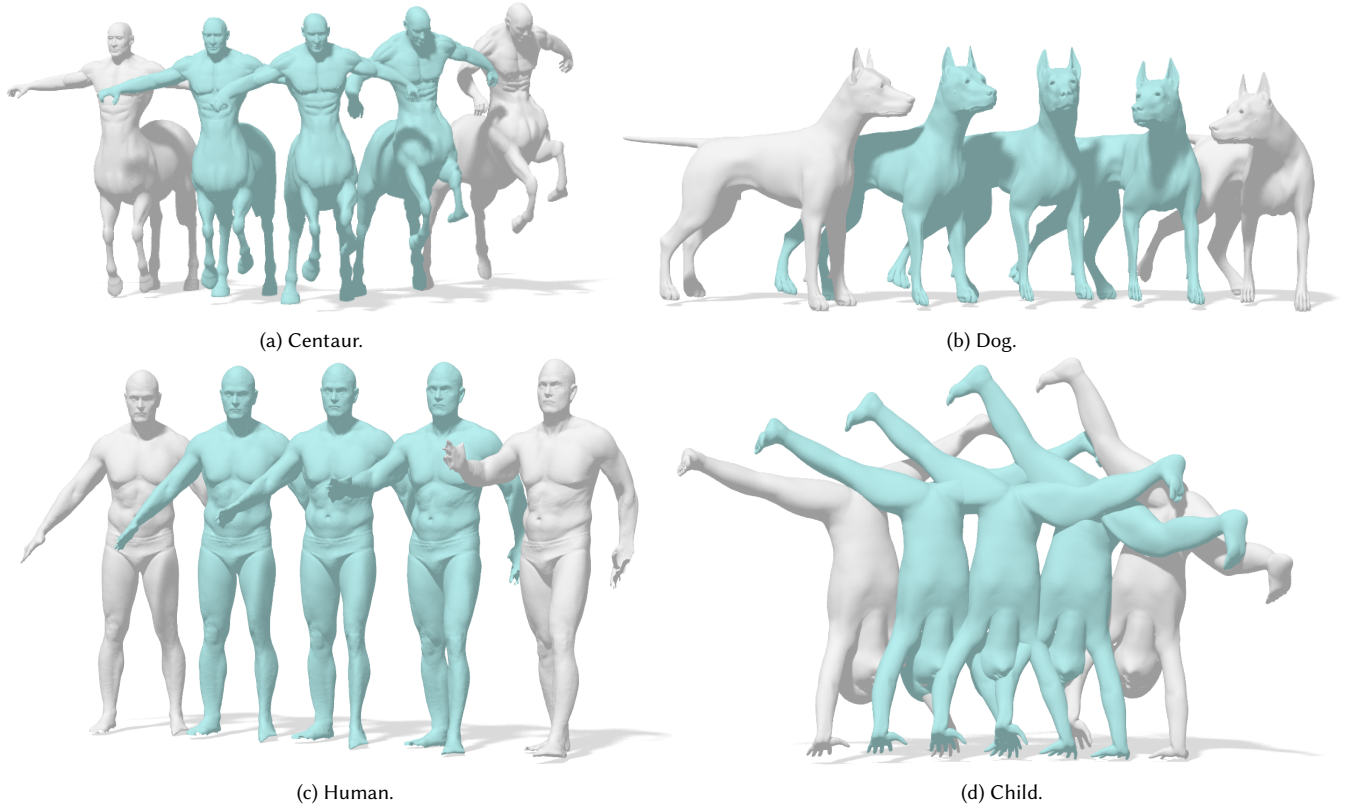


Fig. 2. Some examples of shapes that are morphed into one another according to the initial value problem of Eq. (1). (a) and (b) are from the TOSCA dataset and stem from the quantitative evaluations of our method in Section 7.1. Subfigure (c) is a 214k vertices shape from the FAUST data set on which we evaluated our registration performance in Section 7.2 and (d) from the KIDS dataset [Rodola et al. 2014]. The source and target shape are shown in white and the interpolations at times $t = 0.25, 0.5, 0.75$ in blue. Notice that the translation is not part of our deformation and was only introduced for clarity in the figures.

In the case of $D = 3$ spatial dimensions the construction of v in (5) admits the following form:

$$v = \begin{pmatrix} \partial_2 \Phi_3 - \partial_3 \Phi_2 \\ \partial_3 \Phi_1 - \partial_1 \Phi_3 \\ \partial_1 \Phi_2 - \partial_2 \Phi_1 \end{pmatrix} = \begin{pmatrix} 0 \\ \partial_3 \Phi_1 \\ -\partial_2 \Phi_1 \end{pmatrix} + \begin{pmatrix} -\partial_3 \Phi_2 \\ 0 \\ \partial_1 \Phi_2 \end{pmatrix} + \begin{pmatrix} \partial_2 \Phi_3 \\ -\partial_1 \Phi_3 \\ 0 \end{pmatrix}. \quad (7)$$

5 FRAMEWORK

Regarding relevant applications we will mainly restrict ourselves to the case of $D = 3$. However extensions to higher dimensions or the 2D case are straight forward.

5.1 Spatial representation

We need to describe the velocity fields v in a more tangible manner such that we obtain a computationally feasible method. The problem is that there are infinitely many choices for functions $\Phi \in C^\infty(\Omega, \mathbb{R}^D)$. The most straight-forward approach is choosing a discretization of the embedding space, e.g. with a voxel grid. The potential and deformation fields can then be defined by assigning a three-dimensional vector to every voxel. The problem with this approach is that it has cubic complexity which becomes costly very fast. Furthermore, we do not get a spatially continuous deformation

with this and loose the volume conservation and other desirable properties as a consequence. In the following we will introduce a finite, linear basis $\{v_1, \dots, v_K\}$ for any velocity field on Ω and derive a formulation to restrict it to only span smooth, divergence-free fields. The number of basis function can be adjusted for either speed or expressiveness.

The eigenfunctions of the Laplace-Beltrami operator are often used in shape analysis because of their useful properties like invariance to non-rigid deformations, smoothness and natural ordering. We use a similar basis for smooth, divergence-free vector fields in \mathbb{R}^D . Without loss of generality the considered domain is assumed to be a D -dimensional cube $\Omega := [0, 1]^D$ and we translate and scale any shape to generously fit inside. We start with basis functions $\{\phi_1, \phi_2, \dots\}$ which are the eigenfunctions of the standard Laplacian Δ on Ω :

$$\Delta \phi_k = \lambda_k^\Delta \phi_k. \quad (8)$$

This basis of eigenfunctions $\{\phi_1, \phi_2, \dots\}$ is ordered such that the eigenvalues $0 \geq \lambda_1^\Delta \geq \lambda_2^\Delta \geq \dots$ are descending. Furthermore, we require the Laplacian to admit Dirichlet boundary conditions $\Phi|_{\partial\Omega} = 0$. The ϕ_k can be determined analytically and they are

exactly the sin elements of the Fourier basis:

$$\{\phi_1, \phi_2, \dots\} = \left\{ 2^{\frac{D}{2}} \prod_{d=1}^D \sin(\cdot \pi j_d) \mid (j_1, \dots, j_D) \in \mathbb{N}^D \right\}. \quad (9)$$

Note, that the factor $2^{\frac{D}{2}}$ in front of these basis functions rescales them such that the ϕ_k form an orthonormal basis wrt. the $\|\cdot\|_{L^2(\Omega)}$ norm. The eigenvalue λ_k^Δ of Δ corresponding to the eigenfunction ϕ_k is the following:

$$\lambda_k^\Delta := -\pi^2 \sum_{d=1}^D j_d^2. \quad (10)$$

We can now map the potential basis to the velocity field to obtain a feasible description v . For this purpose we directly insert the basis elements ϕ_k from (9) into the places of Φ_1, \dots, Φ_D in (5). Due to the linearity of the curl operator $\nabla \times \cdot$ this can be performed for every entry of Φ at a time, see (7) for $D = 3$. Overall, we obtain a basis $\{v_1, v_2, \dots\}$ of the velocity field v . In the 3D case it is explicitly defined as:

$$\{v_1, v_2, \dots\} = \bigcup_{k=1}^{\infty} \left\{ \begin{pmatrix} 0 \\ \partial_3 \phi_k \\ -\partial_2 \phi_k \end{pmatrix}, \begin{pmatrix} -\partial_3 \phi_k \\ 0 \\ \partial_1 \phi_k \end{pmatrix}, \begin{pmatrix} \partial_2 \phi_k \\ -\partial_1 \phi_k \\ 0 \end{pmatrix} \right\}. \quad (11)$$

In this context the basis elements v_k are again sorted according to the eigenvalues λ_k^Δ of the corresponding ϕ_k in descending order. Note, that there are in general multiple basis functions v_k for each eigenvalue λ_k^Δ . This yields a feasible description of the velocity field by computing v as a linear combination of the first K basis elements:

$$v(x) = \sum_{k=1}^K v_k(x) a_k. \quad (12)$$

The coefficients a_k can be defined as random variables with a Gaussian prior distribution $a_k \sim \mathcal{N}(0, \lambda_k)$. The weights λ_k are constructed from the eigenvalues λ_k^Δ in the following manner:

$$\lambda_k := (-\lambda_k^\Delta)^{-\frac{D}{2}} = \left(\pi^2 \sum_{d=1}^D j_d^2 \right)^{-\frac{D}{2}}. \quad (13)$$

In Figure 3 the first 3000 eigenvalues λ_k^Δ and weights λ_k are displayed for $D = 3$. Intuitively this kind of weighting promotes a damping of the high frequency components of v and therefore yields a uniform vector field, because the coefficients a_k are sampled with a smaller variance λ_k . This also justifies the truncation in (12), because the weights corresponding to high frequency basis elements are insignificantly small anyway. The mathematical background concerning the particular choice of prior distribution $a_k \sim \mathcal{N}(0, \lambda_k)$ is provided in Appendix A.

The Dirichlet boundary conditions automatically guarantee that there is no flow out of the domain Ω , in the sense that the components of v_k are orthogonal to the outer normals at the boundary $\partial\Omega$. This can be easily verified for the case $D = 3$ by computing the basis elements (11) inserting (9), but we refrain from proving this property here. It also becomes obvious by looking at instances of the velocity basis functions in Figure 4.

The introduced representation of the velocity field has several beneficial properties. On one hand, it can be evaluated at any point in the domain Ω because we do not need to introduce a spatial

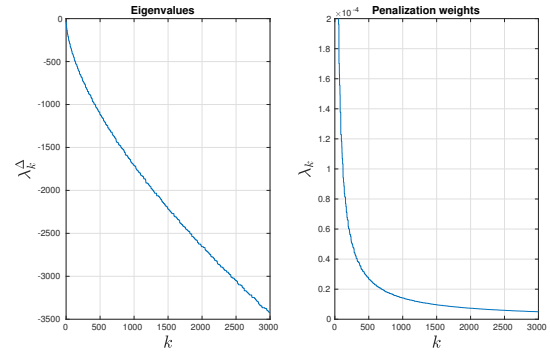


Fig. 3. The first 3000 eigenvalues λ_k^Δ of the Laplacian and the corresponding penalization weights λ_k for the 3D case.

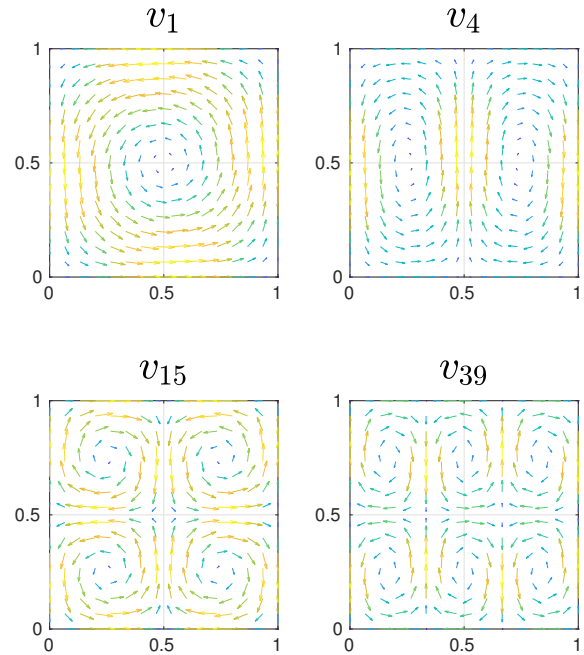


Fig. 4. Cross section of some deformation field basis functions $v_k : \Omega \rightarrow \mathbb{R}^3$ at $x_3 = 0.5$. Notice the low frequency structures for low k and increasing frequencies with higher indices.

discretization. Later we will use this to make our method applicable to very high resolution shapes. On the other hand, the particular weighting of the summands and the truncation in (12) induces an inbuilt low-pass filtering because it favors the low frequency basis elements.

Classical shape registration methods like the iterative closest point (ICP) algorithm [Besl and McKay 1992] determine a rigid transformation between two shapes. Interestingly, our approach

can be interpreted as a direct extension of these transformations. The deformation fields corresponding to translations and rotations are divergence free and fairly uniform, therefore they are by design contained in our framework. This becomes even clearer when the basis function v_1 in Figure 4 is examined. It is fairly similar to a rotation around the x_3 axis. This especially holds near the center of the domain Ω and deteriorates at its boundary $\partial\Omega$, see Appendix B for a thorough investigation of this property. The basis elements v_2 and v_3 are equivalent to v_1 for rotations around the x_2 and x_1 axis. Although we use a rectangular domain the higher order basis functions can account for small deviations. Nevertheless, the considerations in this subsection raise the question whether a cubic domain Ω is the best choice for our purposes. Following the work in [Zhao and Burge 2007], [Zhao and Burge 2008] we could actually pursue our approach in a spherical domain. This would lead to more complex basis functions v_k , but the first three eigenfunctions would exactly span the space of rotations around the center without undesirable artifacts at the boundary of the domain. We believe that this would be beneficial and we intend to investigate this approach in the future, but we refrain from using these basis functions here due their complex structure.

5.2 Temporal discretization

In order to evaluate the correspondence mapping f in (2) we have to approximately solve the initial value problem (1) by a numerical integration scheme. A straightforward choice in this context is the explicit Euler method [Griffiths and Higham 2010], mainly due to its simplicity. We could in theory also use a higher order explicit integration scheme like the Runge-Kutta method [Griffiths and Higham 2010, Ch. 9] but our experiments indicate that the forward Euler method is sufficiently accurate. We therefore subdivide the time space in an equidistant grid with $T \in \mathbb{N}$ intervals. The Euler steps have a step size $h = \frac{1}{T}$. This yields the following explicit iteration scheme:

$$\begin{cases} x_n^{(0)} := x_n. \\ x_n^{(t+1)} := x_n^{(t)} + hv(x_n^{(t)}). \\ f_n := x_n^{(T)} \end{cases} \quad (14)$$

We typically choose $T \in \{1, \dots, 100\}$ in our experiments. In general, we have to make a trade off between runtime and accuracy when selecting a proper number of steps T . We commonly also get meaningful transformations if we choose T to be small but we might lose some key properties of our framework like the volume preservation. This effect is illustrated in Figure 5 for the 2D shape of a bat transformed by a rotational deformation field. In this example one forward Euler steps yields an outward spiral point trajectory which leads to an expansion of the whole shape. Theoretically, we still have this issue for 20 or more steps but its impact becomes insignificant.

6 OPTIMIZATION

Like in [Myronenko and Song 2010] and [Ma et al. 2014] we address the shape registration problem in a probabilistic manner. We formulate the problem as a Gaussian Mixture model (6.1) and simultaneously determine the deformation field coefficients and the

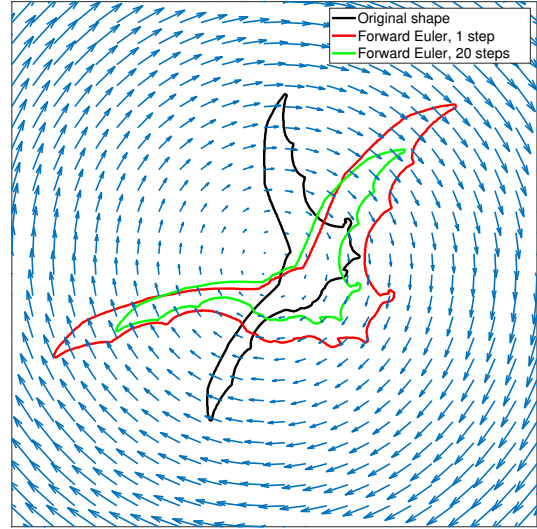


Fig. 5. Two different results of the explicit Euler transformation applied to a bat shape of the MPEG-7 dataset (black). This deformation field corresponds to a rotation and the step size is chosen such that the shape rotates 45 degrees. For one step $T = 1$ the shape expands (red) whereas for $T = 20$ the area of the interior is preserved (green).

correspondence weights by applying an expectation maximization approach (6.2).

6.1 Gaussian mixture model

We interpret the shifted points $f_n = x_n^{(T)}$ as the centers of Gaussian distributions with the covariance matrix $\sigma^2 I_D \in \mathbb{R}^{D \times D}$ which in the end should describe \mathcal{Y} well. Furthermore, each point y_m is assumed to correspond to some point x_n . This relationship is encoded by the correspondence matrix $Z \in \{0, 1\}^{(N+1) \times M}$, where $\sum_{n=1}^{N+1} Z_{nm} = 1$. If $Z_{(N+1)m} = 1$ for some m , the point y_m does not correspond to any point x_n and it is assumed to be uniformly sampled from Ω instead. This way we counteract the effect of outliers by acknowledging their presence and building it into our model.

According to Bayes' theorem the posterior probability distribution of the desired parameters a_k in (12) given the latent correspondences Z_{nm} and the observed points \mathcal{Y} is defined as follows:

$$\begin{aligned} p(a|Z, \mathcal{Y}) &\propto p(a)p(\mathcal{Y}|Z, a) = p(a) \prod_{m=1}^M p(y_m|Z, a) \\ &= p(a) \prod_{m=1}^M \prod_{n=1}^{N+1} p(y_m|Z_{nm} = 1, a)^{Z_{nm}}. \end{aligned} \quad (15)$$

In the context of (12) it was mentioned, that the prior of the parameters a_k is a Gaussian distribution $a_k \sim \mathcal{N}(0, \lambda_k)$. As a shorthand notation we now define the diagonal matrix $L := \text{diag}(\lambda_1, \dots, \lambda_K)$ and set the prior $a \sim \mathcal{N}(0, L)$ for the coefficient vector a . In order

to explicitly evaluate the posterior density of a in (15) we have to investigate the data likelihood $p(y_m|Z_{nm} = 1, a)$ in detail. As we proposed before, for $n < N + 1$ it is constructed to be the density of a Gaussian distribution centered at the shifted points f_n :

$$p(y_m|Z_{nm} = 1, a) = \frac{1}{(2\pi\sigma^2)^{\frac{D}{2}}} \exp\left(-\frac{1}{2\sigma^2}\|y_m - f_n\|_2^2\right). \quad (16)$$

For the case $n = N + 1$ it is simply the density of the uniform distribution, because y_m is considered to be an outlier:

$$p(y_m|Z_{(N+1)m} = 1, a) = 1. \quad (17)$$

6.2 Expectation maximization

We want to determine the coefficients a by applying an expectation maximization approach similar to [Myronenko and Song 2010]. In the E-step soft correspondences $W^{\text{dist}} \in [0, 1]^{(N+1) \times M}$ are determined as a relaxed version of the latent variables Z :

$$\begin{aligned} W_{nm}^{\text{dist}} &= \mathbb{E}_{Z|\mathcal{Y}, a}(Z_{nm}) = p(Z_{nm} = 1|y_m, a) \\ &= \frac{p(y_m|Z_{nm} = 1, a)}{p(y_m|a)} = \frac{p(y_m|Z_{nm} = 1, a)}{\sum_{\tilde{n}=1}^{N+1} p(y_m|Z_{\tilde{n}m} = 1, a)}. \end{aligned} \quad (18)$$

The data likelihood terms $p(y_m|Z_{nm} = 1, a)$ are again defined as proposed in (16) and (17). The M-step now consists of minimizing the following energy with respect to a :

$$\begin{aligned} &\mathbb{E}_{Z|\mathcal{Y}, a}(-\log p(a|Z, \mathcal{Y})) \\ &= -\log p(a) - \sum_{m=1}^M \sum_{n=1}^{N+1} W_{nm}^{\text{dist}} \log p(y_m|Z_{nm} = 1, a) \\ &\propto \frac{1}{2}a^T L^{-1} a + \frac{1}{2\sigma^2} \sum_{m=1}^M \sum_{n=1}^N W_{nm}^{\text{dist}} \|y_m - f_n\|_2^2. \end{aligned} \quad (19)$$

Note that the log likelihood of y_m for the case $n = N + 1$ is simply zero, see (17). In this context the shifted points f_n also depend on the unknown coefficients a . This yields a rather easy optimization task, if we choose $T = 1$. In this case we merely have to perform one forward Euler step in (14), which makes the dependence of $f_n = x_n^{(T)}$ on a linear. The minimization of (19) is then a linear least square problem, which involves solving a $K \times K$ linear system of equations. Therefore, our method can be interpreted as an extension of certain former approaches to point set registration [Ma et al. 2014; Myronenko and Song 2010] modeling the transformation mapping $f : \Omega \rightarrow \mathbb{R}^D$ as linear wrt. some unknown parameters a .

6.3 Feature descriptors

To apply our framework to the shape registration problem we have to determine the weights (E step) and the deformation field parameters (M step) in an alternating manner. In the derivations above we specified how to perform these steps using the pairwise distances of the two pointsets \mathcal{X} and \mathcal{Y} . We will now further improve this approach by incorporating feature descriptors in our model. They initially convey which parts of the shapes correspond to each other and steer it towards a plausible local optimum. Therefore they help to account for correspondence ambiguities, especially in the presence of large scale deformations. Moreover, the use of descriptors also helps to improve the accuracy of our method, because they

encode information about fine scale structures of the considered shapes.

We choose a combination of the heat kernel signature (HKS) [Sun et al. 2009] and SHOT descriptors [F. Tombari and Stefano 2010]. This yields for any pair of points $x_n \in \mathcal{X}$ and $y_m \in \mathcal{Y}$ an estimate $F_{nm} \geq 0$ of how similar these points are according to their local and regional properties. The entries of this feature matrix $F \in \mathbb{R}^{N \times M}$ are constructed to be the sum of squared distances of all feature values at the points x_n and y_m . The formulas (16), (17) and (18) provide a method to compute proper correspondence weights W_{nm}^{dist} using the squared Euclidean distance $\|y_m - f_n\|_2^2$ of the points y_m and f_n . We can now analogously compute the feature distance weights W_{nm}^{feat} using the following construction:

$$W_{nm}^{\text{feat}} := \frac{\exp\left(-\frac{1}{2\tau^2}F_{nm}\right)}{(2\pi\tau^2)^{\frac{D}{2}} + \sum_{\tilde{n}=1}^N \exp\left(-\frac{1}{2\tau^2}F_{\tilde{n}m}\right)}. \quad (20)$$

Note that we simply set $W_{(N+1)m}^{\text{feat}} := 0$. In this context the hyperparameter τ is the variance of the feature distances F_{nm} . We determine a sensible choice for τ by evaluation of the empirical variance of the feature values for some examples. The weights W_{nm}^{feat} can now be added to the distance weights W_{nm}^{dist} to obtain a combined weight W_{nm} :

$$W_{nm} := W_{nm}^{\text{dist}} + \mu W_{nm}^{\text{feat}}. \quad (21)$$

With the parameter μ we can control the influence of the feature weight terms. In our experiments we choose $\mu \in [0.1, 1]$.

6.4 Robust correspondences

We already mentioned in the context of defining the distance matrix W^{dist} in (18) how we incorporated robustness to outliers in our model. However this remedy only works partly, because according to (21) the matrix W also consists of the feature matrix W^{feat} which yields rather noisy correspondences. In order to generally make our method more robust to outliers we will reformulate the correspondence penalization term $\frac{1}{2}\|y_m - f_n\|_2^2$ in (19) to

$$\rho(\|y_m - f_n\|_2). \quad (22)$$

The function $\rho : \mathbb{R} \rightarrow [0, \infty)$ is the Huber loss [Huber 1964]:

$$\rho(r) = \begin{cases} \frac{1}{2}r^2 & |r| \leq r_0. \\ r_0|r| - \frac{1}{2}r_0^2 & \text{otherwise.} \end{cases} \quad (23)$$

We choose the outer slope as $r_0 := 0.01$. For values $\|y_m - f_n\|_2 \leq r_0$ the term (22) remains exactly the same, but for bigger residuals the penalization by the Huber loss only grows linearly. Due to this property the Huber norm does not assert the issue of outliers exorbitantly high and is therefore more robust than the standard least squares loss.

6.5 Algorithm

According to the previous subsections the energy to optimize is the following:

$$E(a) := \frac{1}{2}a^T L^{-1} a + \frac{1}{\sigma^2} \sum_{m=1}^M \sum_{n=1}^N W_{nm} \rho(\|y_m - f_n\|_2). \quad (24)$$

We minimize this energy E with a Gauss-Newton type iteration scheme. A thorough derivation is provided in Appendix C. The complexity of this approach stems from the elaborate dependency (14) of f_n on the deformation parameters a . We already mentioned that we want to perform an expectation maximization algorithm which determines the coefficients a and the weights W in an alternating manner. In order to avoid a nesting of iteration schemes we refrain from computing exact minimizers of E every time we update $a^{(i)}$. Instead we merely perform one Gauss-Newton update step per iteration. The resulting algorithm therefore alternates between determining the weights $W^{(i)}$ according to (21) and computing one Gauss-Newton step to obtain $a^{(i)}$.

7 EXPERIMENTS

We perform experiments for several applications including shape matching and interpolation to show that our method is general and flexible. Although we handle shapes with up to 200k and more vertices, the computation of the deformation field is always done on a downsampled version with 3000 vertices and then applied to the full resolution. We use Euclidean farthest point sampling. When downsampling the subset should include all relevant fine scale structures in order for the deformation field to move these correctly but we found 3000 sufficient for all our applications. As a preprocessing step, we align the shapes using PCA and shift them such that the empirical mean of the point clouds corresponds to the middle of the domain. When averaging over all experiments presented here, our algorithm takes about 400 seconds to compute all correspondences for one pair of shapes. Due to our a priori downsampling this is almost independent of the number of vertices. All experiments were performed with MATLAB on a system with an Intel Core i7-3770 CPU clocked at 3.40GHz, 32 GB RAM and a GeForce GTX TITAN X graphics card running a recent Linux distribution.

7.1 Matching

We verify our method using the TOSCA¹ dataset [Bronstein et al. 2008] which contains 76 triangular meshes. The dataset is divided in 8 classes of humans and animals with several poses each and known intraclass correspondences. We use the HKS [Sun et al. 2009] and SHOT [F. Tombari and Stefano 2010] descriptors to compute the feature correspondence matrix W^{feat} , as specified in (20). In these experiments, we solely operate on the raw shape data and in particular do not need any ground truth information.

The two quantities of interest are initialized to be zero $W^{\text{dist},(0)} := 0$, $a^{(0)} := 0$, therefore the initial correspondence matrix is proportional to the feature matrix $W^{(0)} = \mu W^{\text{feat}}$. We set the hyperparameters $\sigma^2 := 0.01$ and $\mu := 1$ and choose $K = 3000$ basis functions for the deformation field.

Because $W^{(i)}$ only contains 3000 correspondences, we perform a Euclidean nearest-neighbor search to obtain a dense correspondence. The evaluation is done with the Princeton benchmark protocol [Kim et al. 2011]. Given the ground-truth match $(x, y^*) \in \mathcal{X} \times \mathcal{Y}$, the error of the calculated match (x, y) is given by the geodesic distance

¹http://tosca.cs.technion.ac.il/book/resources_data.html

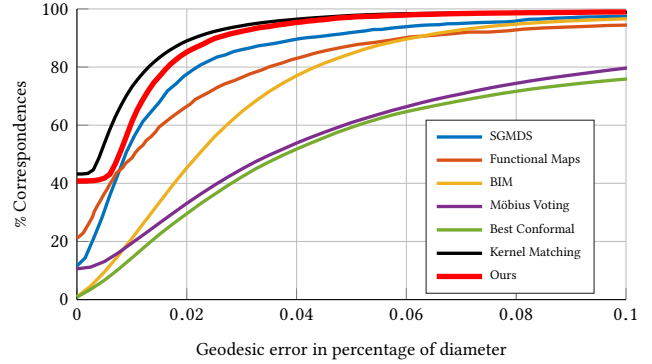


Fig. 6. Quantitative evaluation using the Princeton benchmark protocol on the TOSCA dataset. We compare with Spectral Generalized Multi-Dimensional Scaling [Aflalo et al. 2016], Functional Maps [Ovsjanikov et al. 2012], Blended Intrinsic Maps [Kim et al. 2011], Möbius Voting [Lipman and Funkhouser 2009], Best Conformal Maps [Kim et al. 2011] and Kernel Matching [Vestner et al. 2017].

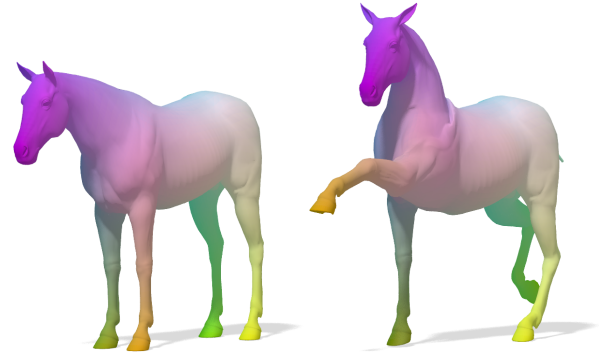


Fig. 7. Example of a correspondence on the horse from the TOSCA data set calculated with our method. Same color means the points were matched with each other.

between y and y^* normalized by the diameter of \mathcal{Y} .

$$\epsilon(x) = \frac{d_{\mathcal{Y}}(y, y^*)}{\text{diam}(\mathcal{Y})}$$

We plot cumulative curves showing the percentages of matches that are below an increasing threshold. As zero is the values for ground-truth matches, the ideal curve would be constant at 100. See Figure 6 for our results and Figure 7 for an example matching.

Close Topology. Our method produces smooth deformation fields in the embedding space which leads to problems when separating (nearly) touching parts because the basis is too low frequency. Since expanding the basis increases the complexity too much, we instead choose to reduce the number of time steps in the simulation. This loosens the volume-preserving property but allows nearly touching deformations. Qualitatively one would call this effect a topological change, although the triangle meshes in TOSCA make a distinction between these connections and parts that actually belong together. Therefore an intrinsic method is by design not affected by such

overlaps. The intuition why this is an issue for our method is the following: The volume preservation of our method also holds for the space between parts of the shape. As two such regions approach each other the method is required to move the volume of the intermediate region out of the way. However, at some point this is not possible anymore, because we assume the deformation fields to be as uniform as possible and its resolution is restricted by the wavelength of the finest eigenfunction in the deformation basis (11). We can of course increase the number of basis functions to counteract this effect at the cost of an increasing execution time but there is another solution to this problem. If we simply choose less time steps we enable the method to do bigger leaps with each step. It turns out that this help to close the gap between two regions such that they can eventually touch. In particular we can e.g. choose $T \in \{1, \dots, 10\}$ instead of $T = 100$ for some extreme cases of topological noise. We partly sacrifice the volume conservation property of our method with this because larger steps render the integration error of the explicit Euler scheme significantly high. Nevertheless, it improves the matching result for these examples.

This leaves us with the task of detecting these topological changes a priori such that our algorithm can choose a proper time step T . For this purpose we define for every pair of points y, y^* of the goal shape \mathcal{Y} the following topology estimate \mathcal{T} :

$$\mathcal{T}(y, y^*) := \left(\frac{d_{\mathcal{Y}}(y, y^*)}{\|y - y^*\|_2} \right)^2 - 1. \quad (25)$$

As before $d_{\mathcal{Y}}(y, y^*)$ is the geodesic distance of y and y^* , therefore \mathcal{T} is non-negative. High values of \mathcal{T} imply, that the geodesic distance of y and y^* is significantly bigger than the Euclidean distance. In our experiments we determine this quantity for a small test set of point pairs for 50 points determined with farthest point sampling. If the sum of these evaluations pass a certain threshold, the algorithm chooses $T = 5$ steps and otherwise it uses $T = 100$ time steps. We want to point out that there is no general way to choose this threshold because it depends severely on the topology of the considered shapes.

7.2 Registration

We apply our framework to the FAUST dataset, which contains data from scans of real humans with different poses. Each of these shapes has approximately $200k$ vertices and some of them are severely affected by topological noise. For these examples we want to demonstrate the advantages of using a spatially fix deformation field. We initialize our method with a sparse set of 30 landmark correspondences and use these to morph all points of one shape onto the other one.

The given 30 landmarks are considered the feature values we use to determine the feature matrix W^{feat} in (20) instead of the HKS and SHOT features. The issue with the later descriptors is that they are severely affected by topological noise and are therefore not applicable for the FAUST scan shapes. In particular $W^{\text{feat}} \in \{0, 1\}^{(N+1) \times M}$ has mostly zero entries except for those which encode the ground truth correspondence information which we set to one. In order for the feature matrix W^{feat} to have the same magnitude as W^{dist} we will set the hyperparameter $\mu := 1000$. Furthermore, we

set $\sigma^2 := 0.01$, $K := 3000$ and we use a temporal discretization of $T = 100$ steps. Again we match the null shape of every person to all its other poses. In Figure 8 we display the surface distance of the morphed shapes to the goal shape for some examples.

7.3 Shape Interpolation

Interpolation. In comparison to other shape matching approaches, our setup models deformations in a comprehensive manner. It has a built in description of the actual transformation shapes undergo over time to morph into one another. In this regard our approach is very similar to movements of deformable objects in the real world. This is additionally supported by the restriction to divergence free deformation fields which yields volume preservation. In this section we want to highlight the advantages of these properties by providing some examples of intermediate configurations.

We already mentioned that our approach can be considered to be the extension of other shape registration methods based on a Gaussian mixture model representation of a point cloud [Myronenko and Song 2010], [Ma et al. 2014]. Those typically try to approximate the point cloud mapping f directly which corresponds to our approach for the choice of $T = 1$ time steps. In particular the quantity f_n depends linearly on the unknowns a and the mapping f for this case admits the following form:

$$f_n := f(x_n) = x_n + \sum_{k=1}^K v_k(x_n) a_k. \quad (26)$$

According to our setup the transformation from x_n to f_n is one forward Euler step. As a consequence the shift (26) of each point x_n over time yields affine linear trajectories. Therefore the intermediate configurations $x^{\text{lin}}(t)$ of the considered point cloud are equivalent to a pointwise linear interpolation:

$$x^{\text{lin}} : \begin{cases} [0, 1] \rightarrow \Omega \\ t \mapsto (1-t)x_n + t f_n. \end{cases} \quad (27)$$

In contrast to this our method produces intermediate points that follow trajectories corresponding to solutions $x(t)$ of an ODE (1). In (2) we made the arbitrary choice of defining the mapped point $f(x_n)$ to be the position of the shifted point at time $t = 1$. We can however also evaluate the solutions of the initial value problem at other times $t \in [0, 1]$. In some sense our approach yields solutions of the shape interpolation problem as a byproduct of computing shape matchings, which emphasizes its strong relation to real world deformations.

We provide concrete examples showing how shapes morph according to our deformation field methodology. For these shapes the ground truth correspondences are known. We therefore refrain from computing them in our algorithm as the purpose of this section is solely to illustrate the interpolation. We will furthermore consider pairs of point clouds \mathcal{X} and \mathcal{Y} with the same number $N = M$ of points, where w.l.o.g. the points x_n and y_n belong to each other. The correspondence matrix W is then simply the identity matrix:

$$W = I_N \in \mathbb{R}^{N \times N}. \quad (28)$$

In this context we use $K = 3000$ basis functions v_1, \dots, v_{3000} and set the hyperparameter $\sigma^2 := 0.01$. We use a temporal discretization

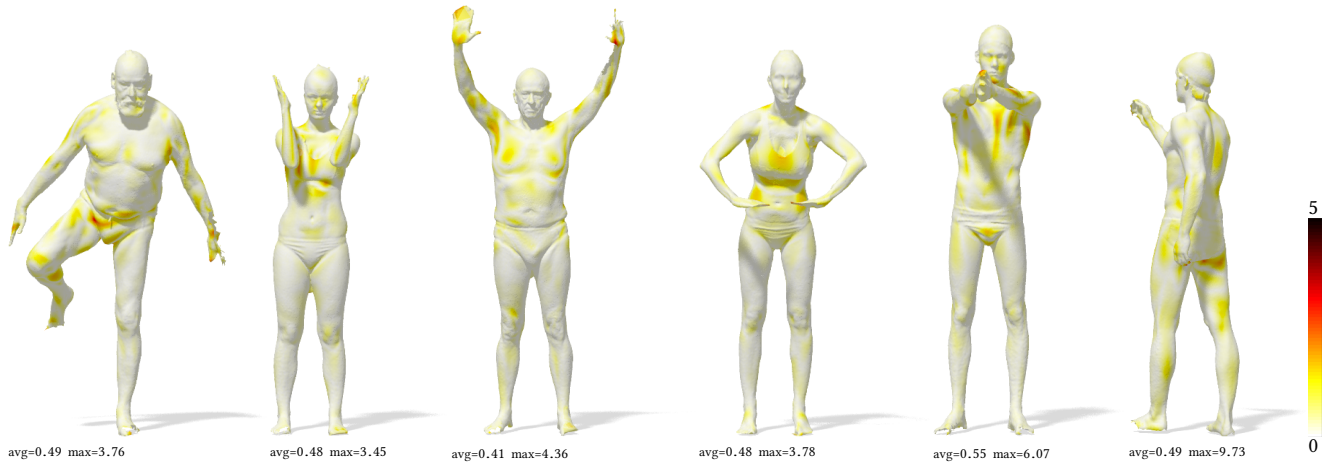


Fig. 8. Example registrations from the FAUST scan data set. The surface color corresponds to the Euclidean surface distance between scan and registration. The scale is the same on all plots. All measures are in cm. We report the average and maximum error under each image.

of $T = 200$ steps. Examples of this qualitative evaluation were already displayed in Figure 2.

The intermediate shapes produced by our method are usually fairly realistic and in particular more meaningful than those resulting from linear interpolation. In order to emphasize this point, we compare the intermediate shapes at time $t = 0.5$ as produced by these two methods in Figure 9. In comparison to our approach, linear interpolation distorts the shapes considerably. Furthermore, the relative size of the subcomponents varies which is inconsistent with transformations in the real world. In contrast to this our method is locally volume preserving. Nevertheless, it can still stretch and bend the shapes. Therefore, it is suitable for modeling shape morphing for rigid, as well as elastic objects. Linear interpolation performs especially bad if the considered transformations include large rotations, see Figure 9.

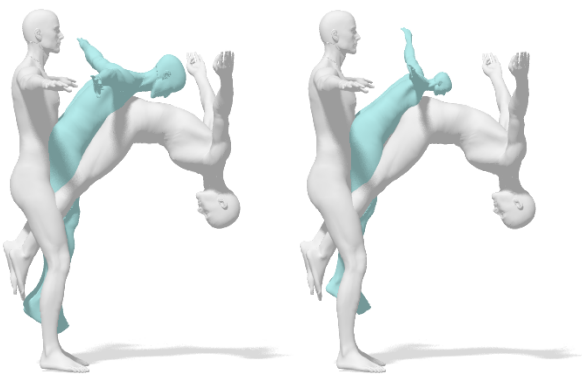


Fig. 9. Comparison of the interpolated shapes at time $t = 0.5$ produced by our method (left) and linear interpolation (right). This is example is hard because the head is rotated by more than 90 degrees in the target. While linear interpolation squeezes the head inbetween our method find a more realistic solution.

Extrapolation. Our extrinsic modeling of deformations has another application. It describes comprehensively for any point in Ω how it has to be shifted over time in order to morph one shape into another one. In particular the underlying deformation field v is independent of the current time t which makes the ODE (1) autonomous. Therefore, we can also use the computed vector field v to determine the solutions of this initial value problem at times $t > 1$, which we demonstrate in Figure 10. The resulting shapes are instances of the shape extrapolation problem. It is obviously an underdetermined task and it is hard to evaluate quantitatively, just like the interpolation problem. However, we observed that the extrapolation shapes our method yields are in many cases quite realistic for moderate timespans $t \in [1, 1.5]$, because of its uniformity and volume conservation. An example of the shape extrapolation using our framework is displayed in Figure 11. In both cases we observe that the speed of the extrapolated shapes seems to slow down after a certain timespan. This effect is observed in those cases where the shape is moving in previously unoccupied space. The algorithm was simply not motivated by the deformation field adaptation in the time interval $t \in [0, 1]$ to impose any particular movement on these regions of the domain Ω . We consider this as desirable behavior due to the inherent ambiguity of the extrapolation problem. Overall the resulting shapes are visually appealing and not too severely affected by distortions.

8 CONCLUSION

We presented a novel method solving the shape correspondence problem while simultaneously computing a smooth, volume-preserving deformation field between the input shapes. Furthermore this deformation can be used to efficiently calculate plausible interpolated shapes between the inputs at any intermediate point in time. The method consists of two parts, the first is the optimization of the deformation field using an expectation maximization approach and the second applies the deformation to the input shapes using an explicit Euler scheme. The big advantage is that a subsampling with around 3000 vertices is sufficient to obtain the deformation field

defined in the continuous embedding space due to our choice of basis. Therefore, the result can be applied to any resolution mesh without slowing the optimization.

We show quantitative results for shape correspondence and registration that can compare to state-of-the-art methods for these specific tasks and examples of shape interpolation and extrapolation that arise naturally from our pipeline.

8.1 Limitations

Due to our choice of basis the deformation field is enforced to be volume preserving. This makes sense in applications with the same

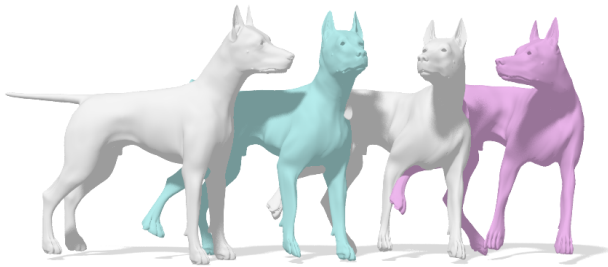


Fig. 10. Example of an extrapolated shape produced by our method. It can be determined using the temporally fixed deformation field v for simulating the initial value problem 1 up to the time $t = 1.3$. Source and target shape are white, one interpolating shape is shown in blue and the extrapolation is pink.



Fig. 11. Example of an extrapolated shapes at the time $t = 1.3$. The details of the hand are squeezed but the overall extrapolation is meaningful. Notice that the deformation field is usually magnified in the area between the input shapes and fans out in several directions further away from the input shapes. Therefore, choosing a really high time does not lead to broken shapes but the movement slows down more and more until it basically stops.

object but prevents inter-object matchings - for example between two humans with different body shapes.

For the same reason, our method has problems with topological changes. Separating two touching parts (for example two hands) is in theory possible but either by using many high frequency deformation basis elements which makes the optimization costly or by using less explicit Euler steps which decrease the quality of the interpolation and accuracy of the final registration.

Since there is not one unique, volume preserving deformation between two shapes, our interpolation is not guaranteed to be as-rigid-as-possible which is plausible in many applications. If the displacement is spatially far, we might end up with squeezed intermediate states that are volume preserving but slightly defy physics.

8.2 Future Work

Right now, the method will always find a solution that is globally volume preserving. This allows to find good deformations fields in the case of serve non-rigid deformations but is not applicable to partial data. In the future, we want to extend this method to work on real scans, for example from the Kinect, which naturally only show partial shapes by making the deformation only locally volume preserving. This might also help with the separation of close parts and handling non volume preserving deformations like style or class changes. Furthermore, we only calculate one field for the entire deformation which means mass at one spatial point always needs to move in the same direction, even at a later time step. This restricts the complexity of the deformations that our method can handle, especially for large-scale motions over a longer period of time. It also leads to problems when non-matching parts of the input shapes overlap in the initialization. Future versions should allow more flexible types of deformation fields to extend it to a broader range of applications. We could for example associate different parts of the shape with different deformations fields or let them vary over time to address more difficult tasks.

REFERENCES

- Yonathan Aflalo, Anastasia Dubrovina, and Ron Kimmel. Spectral generalized multi-dimensional scaling. *IJCV*, 118(3):380–392, 2016.
- T. Albrecht, M. Luthi, and T. Vetter. A statistical deformation prior for non-rigid image and shape registration. *2008 IEEE Conference on Computer Vision and Pattern Recognition*, pages 1–8, 2008.
- Marc Alexa, Daniel Cohen-Or, and David Levin. As-rigid-as-possible shape interpolation. In *Proceedings of the 27th Annual Conference on Computer Graphics and Interactive Techniques, SIGGRAPH '00*, pages 157–164, 2000.
- Rutherford Aris. *Vectors, tensors, and the basic equations of fluid mechanics*. Englewood Cliffs, N.J., Prentice-Hall, 1962.
- John Ashburner. A fast diffeomorphic image registration algorithm. *Neuroimage*, 38(1):95–113, 2007.
- John Ashburner and Karl J Friston. Diffeomorphic registration using geodesic shooting and gauss-newton optimisation. *NeuroImage*, 55(3):954–967, 2011.
- Paul J Besl and Neil D McKay. Method for registration of 3-d shapes. In *Sensor Fusion IV: Control Paradigms and Data Structures*, volume 1611, pages 586–607. International Society for Optics and Photonics, 1992.
- Christoph Bregler, Aaron Hertzmann, and Henning Biermann. Recovering non-rigid 3d shape from image streams. *Proceedings IEEE Conference on Computer Vision and Pattern Recognition*, 2:690–696, 2000.
- Alexander M Bronstein, Michael M Bronstein, and Ron Kimmel. Generalized multi-dimensional scaling: a framework for isometry-invariant partial surface matching. *PNAS*, 103(5):1168–1172, 2006.
- Alexander M Bronstein, Michael M Bronstein, and Ron Kimmel. *Numerical geometry of non-rigid shapes*. Springer, 2008.
- Qifeng Chen and Vladlen Koltun. Robust nonrigid registration by convex optimization. In *IEEE International Conference on Computer Vision (ICCV)*, pages 2039–2047, 2015.

- Alexandre J Chorin and Jerrold E Marsden. *A Mathematical Introduction to Fluid Mechanics*. Springer, 1993.
- Simon L Cotter, Gareth O Roberts, Andrew M Stuart, and David White. Mcmc methods for functions: modifying old algorithms to make them faster. *Statistical Science*, 28(3):424–446, 2013.
- Masoumeh Dashti and Andrew M Stuart. The bayesian approach to inverse problems. *Handbook of Uncertainty Quantification*, pages 311–428, 2017.
- Jürgen Dölz, T Gerig, Marcel Lüthi, Helmut Harbrecht, and Thomas Vetter. Efficient computation of low-rank gaussian process models for surface and image registration. 2017.
- Anastasia Dubrovina and Ron Kimmel. Matching shapes by eigendecomposition of the laplace-beltrami operator. 2010.
- S. Salti F. Tombari and L. Di Stefano. Unique signatures of histograms for local surface description. In *Proceedings ECCV*, 16(9):356–369, 2010.
- Lin Gao, Shu-Yu Chen, Yu-Kun Lai, and Shihong Xia. Data-driven shape interpolation and morphing editing. *Comput. Graph. Forum*, 36:19–31, 2017.
- David Griffiths and Desmond J Higham. *Numerical Methods for Ordinary Differential Equations*. Springer, 2010.
- Behrend Heeren, Martin Rumpf, Peter Schröder, Max Wardetzky, and Benedikt Wirth. Splines in the space of shells. *Computer Graphics Forum*, 35(5):111–120, 2016.
- Peter J Huber. Robust estimation of a location parameter. *Annals of Statistics*, 53(1): 73–101, 1964.
- Vladimir G. Kim, Yaron Lipman, and Thomas A. Funkhouser. Blended intrinsic maps. *Trans. Graphics*, 30(4), 2011.
- Kenneth Levenberg. A method for the solution of certain non-linear problems in least squares. *Quarterly of Applied Mathematics*, 2(2):164–168, 1944.
- Yaron Lipman and Thomas Funkhouser. Möbius voting for surface correspondence. In *Trans. Graphics*, volume 28, page 72, 2009.
- Marcel Lüthi, Christoph Jud, Thomas Gerig, and Thomas Vetter. Gaussian process morphable models. *IEEE Transactions on Pattern Analysis and Machine Intelligence*, 99, 2016.
- Jiayi Ma, Ji Zhao, Jinwen Tian, Alan L Yuille, and Zhuowen Tu. Robust point matching via vector field consensus. *IEEE Transactions on Image Processing*, 23(4):1706–1721, 2014.
- Michael I Miller, Alain Trounev, and Laurent Younes. Geodesic shooting for computational anatomy. *Journal of mathematical imaging and vision*, 24(2):209–228, 2006.
- Andriy Myronenko and Xubo Song. Point set registration: Coherent point drift. *IEEE Transactions on Pattern Analysis and Machine Intelligence*, 32(12):2262–2275, 2010.
- Maks Ovsjanikov, Mirela Ben-Chen, Justin Solomon, Adrian Butscher, and Leonidas Guibas. Functional maps: a flexible representation of maps between shapes. *ACM Transactions on Graphics (TOG)*, 31(4):30, 2012.
- Marco Paladini, Alessio Del Bue, Marko Stosic, Marija Dodig, Joao Xavier, and Lourdes Agapito. Factorization for non-rigid and articulated structure using metric projections. pages 2898–2905, 06 2009.
- E. Rodola, S. Rota Bulo, T. Windheuser, M. Vestner, and D. Cremers. Dense non-rigid shape correspondence using random forests. In *IEEE Conference on Computer Vision and Pattern Recognition (CVPR)*, 2014.
- Emanuele Rodolà, Michael Moeller, and Daniel Cremers. Point-wise Map Recovery and Refinement from Functional Correspondence. In *Vision, Modeling and Visualization*. The Eurographics Association, 2015.
- Joaquim Salvi, Carles Matabosch, David Fofi, and Josep Forest. A review of recent range image registration methods with accuracy evaluation. *Image Vision Comput.*, 25(5):578–596, 2007.
- Andrew M Stuart. Inverse problems: a bayesian perspective. *Acta Numerica*, 19:451–559, 2010.
- T J Sullivan. *Introduction to Uncertainty Quantification*. Springer, 2015.
- Jian Sun, Maks Ovsjanikov, and Leonidas Guibas. A concise and provably informative multi-scale signature based on heat diffusion. In *Computer graphics forum*, volume 28, pages 1383–1392. Wiley Online Library, 2009.
- G. K. L. Tam, Z. Q. Cheng, Y. K. Lai, F. C. Langbein, Y. Liu, D. Marshall, R. R. Martin, X. F. Sun, and P. L. Rosin. Registration of 3d point clouds and meshes: A survey from rigid to nonrigid. *IEEE Transactions on Visualization and Computer Graphics*, 19(7):1199–1217, July 2013.
- Gerald Teschl. *Ordinary Differential Equations and Dynamical Systems*. AMS, 2012.
- Lorenzo Torresani, Aaron Hertzmann, and Christoph Bregler. Nonrigid structure-from-motion: estimating shape and motion with hierarchical priors. *IEEE Transactions on Pattern Analysis and Machine Intelligence*, 30(5):878–892, 2008.
- Oliver van Kaick, Hao Zhang, Ghassan Hamarneh, and Daniel Cohen-Or. A survey on shape correspondence. *Computer Graphics Forum*, 30(6):1681–1707, 2011.
- Amir Vaxman, Christian Müller, and Ofir Weber. Conformal mesh deformations with mÖbius transformations. *ACM Trans. Graph.*, 34(4):55:1–55:11, July 2015.
- M. Vestner, Z. Löhner, A. Boyarski, O. Litany, R. Slossberg, T. Remez, E. Rodolà, A. M. Bronstein, M. M. Bronstein, R. Kimmel, and D. Cremers. Efficient deformable shape correspondence via kernel matching. In *International Conference on 3D Vision (3DV)*, October 2017.
- François-Xavier Vialard, Laurent Risser, Daniel Rueckert, and Colin J Cotter. Diffeomorphic 3d image registration via geodesic shooting using an efficient adjoint calculation. *International Journal of Computer Vision*, 97(2):229–241, 2012.
- Christoph Von-Tycowicz, Christian Schulz, Hans-Peter Seidel, and Klaus Hildebrandt. Real-time nonlinear shape interpolation. *ACM Trans. Graph.*, 34(3):34:1–34:10, May 2015.
- Benedikt Wirth, Leah Bar, Martin Rumpf, and Guillermo Sapiro. A continuum mechanical approach to geodesics in shape space. *International Journal of Computer Vision*, 93(3):293–318, Jul 2011. ISSN 1573-1405. doi: 10.1007/s11263-010-0416-9.
- Dong Xu, Hongxin Zhang, Qing Wang, and Hujun Bao. Poisson shape interpolation. In *Proceedings of the 2005 ACM Symposium on Solid and Physical Modeling*, pages 267–274, 2005.
- Chunyu Zhao and James H Burge. Orthonormal vector polynomials in a unit circle, part i: basis set derived from gradients of zernike polynomials. *Opt. Express*, 15(26): 18014–18024, 2007.
- Chunyu Zhao and James H Burge. Orthonormal vector polynomials in a unit circle, part ii: completing the basis set. *Opt. Express*, 16(9):6586–6591, 2008.

A KARHUNEN-LOËVE EXPANSION OF THE DEFORMATION FIELD

We will now provide some theoretical justification for the particular choice of basis in (11) and the construction of the weights (13). These λ_k can be interpreted to be the eigenvalues of the linear operator $C := (-\Delta)^{-\frac{D}{2}}$ corresponding to the eigenfunctions ϕ_k . We can then apply the so-called Karhunen-Loève expansion [Sullivan 2015, Ch. 11] to our setup. This framework provides us with an alternative representation of the potential field Φ , which can in turn be used to define the deformation field v . For further reference concerning the mathematical foundation of this approach the interested reader is referred to [Stuart 2010], [Cotter et al. 2013], [Dashti and Stuart 2017]. Following this approach one can now derive a construction which enables us to sample arbitrary square integrable scalar fields $\hat{\Phi} : \Omega \rightarrow \mathbb{R}$:

$$\hat{\Phi}(x) = \sum_{k=1}^{\infty} \phi_k(x) \sqrt{\lambda_k} \xi_k. \quad (29)$$

According to the Karhunen-Loève expansion the coefficients $\xi_k \sim \mathcal{N}(0, 1)$ are samples of the standard normal distribution. This approach can now be applied to get an alternative description of each entry of the potential vector field Φ . Inserting this in (5) we obtain an alternative representation of the deformation field v . In particular we get the summation (12) for the basis elements (11) in the 3D case. Indeed we can derive the following Gaussian prior distribution for the weights a_k :

$$a_k = \sqrt{\lambda_k} \xi_k \sim \mathcal{N}(0, \lambda_k). \quad (30)$$

The choice of the exponent $\frac{D}{2}$ in the definition of the weights λ_k (13) is not arbitrary. In general it is supposed to be chosen strictly larger than $\frac{D}{2}$ in order for our resulting basis to fulfill certain approximation properties in the limit of infinitely many basis functions, see [Dashti and Stuart 2017, Ch. 2.4]. However we achieved good results in our experiments by choosing it as small as possible in order to not suppress the high frequencies more severely than necessary. In particular the expressiveness of or method seems to deteriorate when a large exponent is chosen, because then the weights (13) decay too rapidly. Therefore we typically even set it to $\frac{D}{2}$ which works fine for our purposes, although this is not theoretically justified when the number of basis functions approaches infinity. On the other hand, choosing it smaller than $\frac{D}{2}$ certainly causes the expected value of the velocity series to diverge for $K \rightarrow \infty$.

To conclude this section we want to motivate our choice of the Karhunen-Loève framework and the particular linear operator C to model the deformation fields v . In the context of the Karhunen-Loève expansion the operator C is called covariance operator. It is typically chosen to incorporate some assumptions about the regularity of the produced sample functions. A natural assumption about the deformation fields v is that they are as uniform as possible. This yields that the resulting correspondence mappings are to some degree spatially continuous. Therefore we require the Dirichlet energy to be small:

$$\|\nabla v\|_{L_2}^2 = \sum_{d=1}^D \int_{\Omega} \|\nabla v_d(x)\|_2^2 dx. \quad (31)$$

We can achieve this by penalizing the high frequency components of v . These frequencies are strongly related to those of the potential field Φ , because according to (5) the basis elements are simply mapped onto the velocity basis elements. This mapping does not change the frequencies:

$$\|\nabla v\|_{L_2} = \|\nabla(\nabla \times \Phi)\|_{L_2} = \|\nabla \Phi\|_{L_2}. \quad (32)$$

If we choose e.g. $D = 2$ one can prove that the Dirichlet energy $\|\nabla v\|_{L_2}^2$ is equivalent to the squared ℓ_2 norm of the weights ξ :

$$\|\xi\|_{\ell_2}^2 = \|\nabla v\|_{L_2}^2, \text{ for } D = 2. \quad (33)$$

A derivation of this property can be found in [Dashti and Stuart 2017, Ch. 7.1.3]. In the case of finitely many parameters ξ_1, \dots, ξ_K the norm $\|\xi\|_{\ell_2}$ is equivalent to the Euclidean norm $\|\xi\|_2$ of the vector $\xi = (\xi_1, \dots, \xi_K)^T$. The term $\|\xi\|_2^2$ is in turn proportional to the negative log likelihood of the standard normal distributed parameter $\xi \sim \mathcal{N}(0, I_K)$:

$$-\log(p(\xi)) = \frac{K}{2} \log(2\pi) + \frac{1}{2} \|\xi\|_2^2 \propto \frac{1}{2} \|\xi\|_2^2. \quad (34)$$

This indicates that a maximum likelihood approach involving ξ leads to an enforcement of uniformity of the vector field v . This can be extended to the case $D = 3$ in a similar manner, but we refrain from providing more details here for the sake of brevity.

B RIGID DEFORMATIONS

A convenient property of the proposed framework is that it models rigid deformations fairly accurately even in the presence of very few basis elements. Note that mere translations are excluded from our considerations here because they are commonly not covered by the Karhunen-Loève expansion and are therefore not included in (12). The components of the velocity basis elements v_k need to have mean zero because otherwise they would induce flow out of the domain Ω :

$$\int_{\Omega} (v_k)_d dx = 0. \quad (35)$$

This is not an issue though because we can simply shift the point clouds a priori such that their empirical mean corresponds to the center of the domain Ω .

It is well known that any rotation around the origin of \mathbb{R}^3 can be decomposed into rotations around the three coordinate axes. Now

consider e.g. the Lie algebra corresponding to the rotation around the z-axis, which is given as follows:

$$\mathfrak{so}_z(3) = \left\{ h \begin{pmatrix} 0 & -1 & 0 \\ 1 & 0 & 0 \\ 0 & 0 & 0 \end{pmatrix} \middle| h \in \mathbb{R} \right\}. \quad (36)$$

The elements of the Lie algebra $\mathfrak{so}_z(3)$ correspond to the temporal derivative \dot{x} of the position x . According to (1) this is equivalent to the velocity field $v = \dot{x}$.

If we linearize the sin and cos factors at the center of the domain Ω , we can rewrite the first basis function v_1 of v in the following manner:

$$\begin{aligned} v_1 &= \begin{pmatrix} \partial_2 \phi_1 \\ -\partial_1 \phi_1 \\ 0 \end{pmatrix} = 2^{\frac{D}{2}} \pi \begin{pmatrix} -\sin(\pi x_1) \cos(\pi x_2) \sin(\pi x_3) \\ \cos(\pi x_1) \sin(\pi x_2) \sin(\pi x_3) \\ 0 \end{pmatrix} \\ &= 2^{\frac{D}{2}} \pi^2 \begin{pmatrix} -(x_2 - 0.5) \\ x_1 - 0.5 \\ 0 \end{pmatrix} + \mathcal{O}\left(\left\|x - \begin{pmatrix} 0.5 \\ 0.5 \\ 0.5 \end{pmatrix}\right\|^2\right). \end{aligned} \quad (37)$$

This approximation of v_1 is then equivalent to $\mathfrak{so}_z(3)$ corresponding to a z-axis rotation around the center $(0.5, 0.5, 0.5)^T$:

$$\begin{pmatrix} -(x_2 - 0.5) \\ x_1 - 0.5 \\ 0 \end{pmatrix} = \begin{pmatrix} 0 & -1 & 0 \\ 1 & 0 & 0 \\ 0 & 0 & 0 \end{pmatrix} \begin{pmatrix} 0.5 \\ 0.5 \\ 0.5 \end{pmatrix}. \quad (38)$$

These considerations analogously hold for $\mathfrak{so}_x(3)$ and $\mathfrak{so}_y(3)$. Therefore the rigid rotations around the center of the domain are approximately covered by the first 3 basis elements v_1, v_2, v_3 . Note that this linear approximation is fairly accurate at the center of the domain but deteriorates near its bounds $\partial\Omega$ due to the effects of the Dirichlet boundary condition. This is displayed in Figure 4, top-left showing the cross section of the first basis element v_1 at $x_3 = 0.5$.

C OPTIMIZING FOR THE DEFORMATION FIELD WITH GAUSS-NEWTON

According to (12) the deformation field v is exactly determined by the coefficient vector $a \in \mathbb{R}^K$ for the representation we use. In order to compute the optimal deformation parameters a we have to minimize the energy $E(a)$ defined in (24). For this purpose we will first discuss how to optimize the following energy, where the robust Huber loss was replaced by the standard least squares loss:

$$E^{\text{LS}}(a) := \frac{1}{2} a^T L^{-1} a + \frac{1}{2\sigma^2} \sum_{m=1}^M \sum_{n=1}^N W_{nm} \|y_m - f_n\|_2^2. \quad (39)$$

We assume in this context that the correspondence W are fixed. For this optimization we incorporate a Gauss-Newton type method which yields an iteration scheme converging to a local minimum of E^{LS} . Like in the Levenberg-Marquardt algorithm [Levenberg 1944] the iteration will contain an additional damping term L^{-1} which is added to the Hessian of the non-linear least squares term.

Applying the standard Gauss-Newton methodology we get an iterative method to determine the weights a . The general idea of this approach is that the shifted points $f_n(a)$ are linearized around

the current iterate $a^{(i)}$ in the energy (39):

$$E^{\text{LS}}(a) \approx \frac{1}{2} a^T L^{-1} a + \frac{1}{2\sigma^2} \sum_{m=1}^M \sum_{n=1}^N W_{nm} \|y_m - \underbrace{(f_n(a^{(i)}) + D_a f_n(a^{(i)})(a - a^{(i)}))}_{\approx f_n(a)}\|_2^2. \quad (40)$$

This approximate energy is linear in the current unknown a so the remaining task is a simple linear least squares problem. The recursion formula to compute the approximate deformation parameters $a^{(i)}$ then admits the following explicit form:

$$a^{(i+1)} := a^{(i)} - (J^T \tilde{W} J + \sigma^2 L^{-1})^{-1} (J^T r - \sigma^2 L^{-1} a^{(i)}). \quad (41)$$

In this context J consists of the Jacobians of f_n , r of the (weighted) distance residuals and \tilde{W} is a diagonal matrix containing the column sums of W . Let $e_D = (1, \dots, 1)^T \in \mathbb{R}^D$, $e_M = (1, \dots, 1)^T \in \mathbb{R}^M$, then these quantities are explicitly defined as:

$$J = \begin{pmatrix} D_a f_1 \\ \vdots \\ D_a f_N \end{pmatrix} \in \mathbb{R}^{ND \times K}. \quad (42a)$$

$$r = \begin{pmatrix} \sum_{m=1}^M W_{1m} (f_1 - y_m) \\ \vdots \\ \sum_{m=1}^M W_{Nm} (f_N - y_m) \end{pmatrix} \in \mathbb{R}^{ND}. \quad (42b)$$

$$\tilde{W} = \text{diag}(W e_M) \otimes e_D = \text{diag} \begin{pmatrix} e_D \sum_{m=1}^M W_{1m} \\ \vdots \\ e_D \sum_{m=1}^M W_{Nm} \end{pmatrix} \in \mathbb{R}^{ND \times ND}. \quad (42c)$$

What is left to specify is how to compute the derivatives $D_a f_n \in \mathbb{R}^{D \times K}$ in (42a). Note, that $f_n = x_n^{(T)}$ is recursively defined in (14) and differentiating f_n wrt. a is not entirely trivial. However it can be done in a straightforward manner by applying the chain rule to each element of the recursion. As a result the derivative $D_a x_n^{(t)}$ is passed from the first time step $t = 0$ to the last $t = T$ and gradually modified in each step. Inserting the Karhunen-Loève representation (12) in the definition (14) yields the following recursive formula:

$$x_n^{(t+1)}(a) := x_n^{(t)}(a) + h \sum_{k=1}^K v_k(x_n^{(t)}(a)) a_k. \quad (43)$$

The dependencies on a are denoted explicitly in order to make it more comprehensible. The quantities $x_n^{(t)}(a)$ can now be differentiated wrt. a :

$$D_a x_n^{(0)} = 0. \quad (44a)$$

$$D_a x_n^{(t+1)} = \left(I_D + h \sum_{k=1}^K D_x v_k(x_n^{(t)}(a)) a_k \right) D_a x_n^{(t)} + h \begin{pmatrix} | & & | \\ v_1(x_n^{(t)}(a)) & \dots & v_K(x_n^{(t)}(a)) \\ | & & | \end{pmatrix}. \quad (44b)$$

Note that the Jacobian $D_x v_k \in \mathbb{R}^{D \times D}$ can be computed analytically for any basis element v_k . In this context $I_D \in \mathbb{R}^{D \times D}$ is the identity matrix.

The only thing left to discuss is how to extend this approach for the Huber loss penalization version of the energy E in (24). For point distances $\|y_m - f_n\|_2 \leq r_0$ the Huber loss and the least squares loss are the same. For residual values $\|y_m - f_n\|_2 > r_0$ the derivative wrt. the deformation parameters a is the following:

$$D_a \rho(\|y_m - f_n\|_2) = r_0 \frac{(f_n - y_m)^T}{\|f_n - y_m\|_2} D_a f_n. \quad (45)$$

This eliminates the possibility of a direct Gauss-Newton type optimization which requires non linear least squares terms. We can however incorporate this in our algorithm using a simple heuristic. For this purpose we multiply the respective weights W_{nm} with the factor $r_0 \frac{1}{\|f_n - y_m\|_2}$, if $\|y_m - f_n\|_2 > r_0$.